arXiv:cond-mat/0502583v1 [cond-mat.mtrl-sci] 24 Feb 2005

Nanoparticle size distribution estimation by full-pattern powder diffraction analysis.

A. Cervellino*
Laboratory for Neutron Scattering, Paul Scherrer Institute, CH-5232 Villigen PSI, Switzerland

C. Giannini† and A. Guagliardi and M. Ladisa
Consiglio Nazionale delle Ricerche, Istituto di Cristallografia (CNR-IC), Via Amendola 122/O, I-70126 Bari, Italy.

(Dated: March 23, 2022)

The increasing scientific and technological interest in nanoparticles has raised the need for fast, efficient and precise characterization techniques. Powder diffraction is a very efficient experimental method, as it is straightforward and non-destructive. However, its use for extracting information regarding very small particles brings some common crystallographic approximations to and beyond their limits of validity. Powder pattern diffraction calculation methods are critically discussed, with special focus on spherical particles with log-normal distribution, with the target of determining size distribution parameters. A 20-nm CeO_2 sample is analyzed as example.

PACS numbers: 61.10.Nz, 81.07.Bc, 61.46.+w

I. INTRODUCTION

We are assisting at a booming expansion of nanoparticle research and technology. Synthesis method especially make fast progresses[1]. Analysis methods, however, are not up to speed. A fundamental simple task as determining and controlling the size distribution of nanoparticles (NPs hereafter) is currently a complex experimental work, involving electron microscopy and combined techniques. In this work we want to highlight the possibilities offered in this issue by a much less complex technique as powder diffraction.

Powder diffraction is a widespread technique with a great potential to meet the increasing demands of microstructural material characterization. The methods of powder diffraction data analysis have reached maturity for micrometer-sized polycrystalline materials. However, when the particle size falls much below 100 nm, specifically tuned methods of analysis are needed to extract meaningful information from powder diffraction patterns. In fact, nanoparticles (NPs hereafter) present unique analytical challenges. In the most complex cases, non-crystallographic structures[2,3,4,5,6,7,8,9,10,11] may occur. Surface-related deformation fields[12,13,14] are another challenge. In these extreme cases, the classical crystallographic formalism becomes quite useless. The Debye scattering function[15] (that is, the direct evaluation of the NP structure factor from the interatomic distances) is the only choice in those cases. We are currently developing[10,16] methods to increase the efficiency of such calculations and make them a practical tool.

Even for crystalline NPs, however, the small size plays a decisive role. Bragg peaks may be so much broadened that they cannot be simply separated and many approximations, commonly accepted for micrometer size domains, fail. As we will show, also models specifically corrected for NPs[17,18,19] may fail for ultra-small NPs (say below 5 nm diameter, as it will be better specified). Again for these ultra-small sizes the Debye scattering function is the only choice for obtaining precise results, while the smaller number of atoms makes it extremely practical.

The plan of the paper is the following. In Sec. II we discuss the shape-based method for calculating NP powder patterns in relation to the surface structure and to its limits of validity at small sizes. Application to full-pattern fit on a test-case (20-nm CeO_2) is shown in Sec. III.[42] Summary and conclusions are given in Sec. IV.

II. POWDER PATTERNS AND SIZE INFORMATION

Scherrer's formula[20] is the most known method for extracting size information from powder patterns (namely, from the Bragg peaks' width). This is a simple method, but accurate only to the order of magnitude. However, since Scherrer's work, line profile analysis has made enormous progress[21,22,23,24,25,26,27,28,29,30].

Theoretical progress on understanding the physical origin of peak broadening has been focused on the dislocation analysis, size broadening being considered as a side effect to be corrected for in order to determine the defect structure. Nevertheless, today it is possible to determine the parameters of a (log-normal) size distribution of crystallites, together with information on type and concentration of dislocations. These methods are, however, complex and sophisticated, requiring a fairly high signal-to-noise ratio, low and flat background, a precise deconvolution of the instrumental broadening and especially well-isolated Bragg peaks.

Full-pattern fitting methods (*cf.* Sec. II A) are more direct and robust, especially when the target is the size analysis. Firstly, they use all the experimental information, regardless of partial or total peak overlap, increasing redundancy and therefore precision and decreasing experimental requirement. Furthermore, they allow the evaluation of a NP-characteristic feature, namely the variation with size of the lattice parameter[10,11] (an effect that can be important below 20 nm). Corrections for texture,

microabsorption, anisotropic elastic peak shifts and instrumental broadening can also be implemented.

An efficient and precise method to evaluate NP diffraction patterns is needed to perform full-pattern fits. Hereafter we discuss the shape-based method[17,18,19] with a thorough analysis of its validity limits.

A. NP shape-based diffraction models

We shortly recall some methods for the calculation of the powder diffraction intensity for a NP with known periodic structure and definite size and shape. In the following the length of a vector $\boldsymbol{v}$ will be denoted by v. Accordingly, $\boldsymbol{q}$ will be the scattering vector of length $q = 2\sin\theta/\lambda$, where θ is the scattering half-angle and λ the incident wavelength; $\boldsymbol{h}$ shall denote the scattering vector associated with a Bragg peak, its length being h. A NP occupies a geometrical region of space G. We recall[31,32] the definition of a shape function $S(\boldsymbol{r})$, such that $S(\boldsymbol{r}) = 1$ if $\boldsymbol{r}$ lies inside G, $S(\boldsymbol{r}) = 0$ otherwise. We shall hereforth suppose that $S(-\boldsymbol{r}) = S(\boldsymbol{r})$ so that its Fourier transform is real.

However, defining the shape of a crystal means also to describe what happens to the atoms on the surface. These are increasingly important at very small sizes. In fact, there are different ways of interpreting the action of $S(\boldsymbol{r})$, the most meaningful ones being:

a) truncating sharply the scattering density (the electron density for x-rays) at the surface[31,32];

b) selecting all whole unit cells whose origins are in G and all whole atoms whose centres lie in the selected cells[33];

c) selecting all whole atoms whose centres are in G.

Useful illustrations are found in Fig. 1 of Ref. 17 (see Figs. 1a, 1c and 1d, respectively for a, b, c).[43] To evaluate the diffracted intensities, in cases b), c), one may utilize the Debye function. In this way the chosen model is faithfully represented. It is possible, however, to proceed in a different way, that is, by the shape-function method. Accordingly, we first evaluate the scattering amplitude $A(\boldsymbol{q})$. The explicit expressions[17] are, for cases a,b,c:

$$A^{\mathrm{a}}(\boldsymbol{q}) = \sum_{\boldsymbol{h}\in\Lambda^*} \tilde{S}(\boldsymbol{q}-\boldsymbol{h})F(\boldsymbol{h}), \tag{1}$$

$$A^{\mathrm{b}}(\boldsymbol{q}) = \sum_{\boldsymbol{h}\in\Lambda^*} \tilde{S}(\boldsymbol{q}-\boldsymbol{h})F(\boldsymbol{q}), \tag{2}$$

$$A^{\mathrm{c}}(\boldsymbol{q}) = \sum_{\boldsymbol{h}\in\Lambda^*} \tilde{S}(\boldsymbol{q}-\boldsymbol{h})F(\boldsymbol{h},q), \tag{3}$$

where Λ^* is the reciprocal lattice; $\tilde{S}(\boldsymbol{q})$ is the Fourier transform[44] of $S(\boldsymbol{r})$, or

$$\tilde{S}(\boldsymbol{q}) = \int_{\mathbb{R}^3} \mathrm{d}^3\boldsymbol{r} S(\boldsymbol{r})\mathrm{e}^{2\pi i\boldsymbol{q}\cdot\boldsymbol{r}} = \int_G \mathrm{d}^3\boldsymbol{r}\,\mathrm{e}^{2\pi i\boldsymbol{q}\cdot\boldsymbol{r}}\ , \tag{4}$$

and it satisfies $\tilde{S}(\boldsymbol{q}) = \tilde{S}(-\boldsymbol{q})$ because $S(-\boldsymbol{r}) = S(\boldsymbol{r})$; $F(\boldsymbol{h})$ is the unit cell structure factor

$$F(\boldsymbol{h}) = \sum_{\alpha=1}^{N_a} f_\alpha(h)\mathrm{e}^{2\pi i\boldsymbol{h}\cdot\boldsymbol{r}_\alpha}\ , \tag{5}$$

where the sum index α runs on the atoms in the unit cell, which have form factors f_α and position vectors (relative to the cell origin) $\boldsymbol{r}_\alpha$; $F(\boldsymbol{q})$ is the same as the former but evaluated in $\boldsymbol{q}$; and $F(\boldsymbol{h},q)$ is the mixed expression

$$F(\boldsymbol{h},q) = \sum_{\alpha=1}^{N_a} f_\alpha(q)\mathrm{e}^{2\pi i\boldsymbol{h}\cdot\boldsymbol{r}_\alpha}\ . \tag{6}$$

It is evident that form a) is simpler but by construction less reasonable - for electron and x-ray diffraction - than b) and c). In fact, the sharp truncation of the electron density at the surface is unjustified. For neutron nuclear elastic scattering the atoms are point scatterers, therefore, construction a) coincides with c). Accordingly, in the neutron case, the atomic form factors are constant and $A^{\mathrm{a}}(\boldsymbol{q}) = A^{\mathrm{c}}(\boldsymbol{q})$.

Form b) depends on an appropriate choice of the unit cell. Clearly, it preserves the stoichiometric composition and symmetry.

Form c) needs a careful implementation (regarding the definition of G) to preserve stoichiometry, that is important for ionic compounds; however, it is clearly more flexible. Remark also that, in the case of monoatomic lattices, instead - as for simple-cubic, face-centered or body-centered cubic metals - construction b) and c) will be coincident and $A^{\mathrm{b}}(\boldsymbol{q}) = A^{\mathrm{c}}(\boldsymbol{q})$.

B. NP scattering intensities

Squaring Eqs. (1,2,3) we obtain the intensities. Supposing S centrosymmetric and $\tilde{S}$ real, we have

$$I^{\mathrm{a}}(\boldsymbol{q}) = \sum_{\boldsymbol{h}\in\Lambda^*} \tilde{S}^2(\boldsymbol{q}-\boldsymbol{h})\,|F(\boldsymbol{h})|^2\,, \tag{7}$$

$$I^{\mathrm{b}}(\boldsymbol{q}) = |F(\boldsymbol{q})|^2 \sum_{\boldsymbol{h}\in\Lambda^*} \tilde{S}^2(\boldsymbol{q}-\boldsymbol{h}), \tag{8}$$

$$I^{\mathrm{c}}(\boldsymbol{q}) = \sum_{\boldsymbol{h}\in\Lambda^*} \tilde{S}^2(\boldsymbol{q}-\boldsymbol{h})\,|F(\boldsymbol{h},q)|^2\,. \tag{9}$$

Here, we have neglected cross-summations of the form

$$\mathcal{R}(\boldsymbol{q}) = \sum_{\substack{\boldsymbol{h},\boldsymbol{k}\in\Lambda^* \\ \boldsymbol{k}\neq\boldsymbol{h}}} \tilde{S}(\boldsymbol{q}-\boldsymbol{h})\tilde{S}(\boldsymbol{q}-\boldsymbol{k})M^{\mathrm{x}}_{\boldsymbol{q},\boldsymbol{h}}\overline{M}^{\mathrm{x}}_{\boldsymbol{q},\boldsymbol{k}} \tag{10}$$

where overbar stands for complex conjugate and, for x=a,b,c, respectively, it is $M^{\mathrm{a}}_{\boldsymbol{q},\boldsymbol{h}} = F(\boldsymbol{h})$, $M^{\mathrm{b}}_{\boldsymbol{q},\boldsymbol{h}} = F(\boldsymbol{q})$ or $M^{\mathrm{c}}_{\boldsymbol{q},\boldsymbol{h}} = F(\boldsymbol{h},q)$. Neglecting $\mathcal{R}(\boldsymbol{q})$ is, first of all, a question of convenience, because its evaluation - either analytical or numerical - is a nightmare.

There are obvious reasons for neglecting $\mathcal{R}(\boldsymbol{q})$ for large particles. Consider a spherical particle with cubic structure with lattice parameter a and radius $R \gg a$. $\tilde{S}(\boldsymbol{q})$ is large only for $q \lesssim 1/R$, and decreases as $(2\pi qR)^{-2}$ for $q \gg 1/R$. As for any Bragg peak $\boldsymbol{h}$ it is $1/R \ll 1/a \lesssim h$, $\mathcal{R}(\boldsymbol{q}) \sim O((R/a)^{-2})$ can be neglected.

For smaller particles the situation is different. In Refs. 17,33 it is proposed that $\mathcal{R}(\boldsymbol{q})$ is negligible due to a certain statistical 'smearing' of the NP surface region on a thickness of the order of the lattice parameter a. However, this hypothesis cannot be accepted by default.

Firstly, the order at the surface strongly depends on the considered crystal phase and on the actual sample. Consider that for a NP of diameter $D = Na$, the fraction of atoms included in a layer of thickness a is $\approx 6/N$ (about 50% at $D = 10a$, still 12% at $D = 50a$). The structure of this large fraction should be carefully considered on a case-by-case basis. Relaxations in the core due to a disordered layer of thickness a should also be considered. Secondly, supposing a default smearing of the NP boundaries flattens the different construction principles of forms a, b, c. In fact, the differences among them regard the finest details of the NP surface structure.

We shall hereafter assess the effect of neglecting $\mathcal{R}(\boldsymbol{q})$ on the calculation of a powder diffraction pattern. In App. we carry out some relevant calculations. Evidently this will depend on the choice of form a, b, or c. Examples are reported in the following section.

For form $I^{\mathrm{b}}(\boldsymbol{q})$ it turns out that, even when $\mathcal{R}(\boldsymbol{q})$ is not negligible, it yields a contribution that is approximately proportional to the retained term $I^{\mathrm{b}}(\boldsymbol{q})$ of the scattered intensity. This means that the effect of neglecting $\mathcal{R}(\boldsymbol{q})$ may be just a small error on the global scale factor for samples composed of particles of equal size. However, as this effect is size-dependent, it may hamper the evaluation of size distribution when this is not very narrow. A size-related correction factor for the scale factor may - and should - be evaluated (see App.) in this case. This of course is an undesired complication.

In cases a) and c) the neglected term $\mathcal{R}(\boldsymbol{q})$ depends on the crystal structure (see App.). It is not a constant scale factor for all Bragg peaks, and it may have a significant gradient in the Bragg peak positions. At very small sizes the latter may induce a systematic error also in the lattice constant determination. However, in the x-ray case, for form a) $\mathcal{R}(\boldsymbol{q})$ is larger - and has a larger gradient in the Bragg peak neighbourhood - than the corresponding term for form c).

C. NP powder patterns

To obtain a powder diffraction pattern, we must integrate $I^{\mathrm{x}}(\boldsymbol{q})$ (x=a,b,c, see Eqs. (1,2,3)) at constant q. We write $\boldsymbol{q}$ in polar coordinates as $\boldsymbol{q} = (q\sin\psi\cos\phi, q\sin\psi\sin\phi, q\cos\psi) \equiv (q,\omega)$, where ω is the orientation defined by the pair (ψ,ϕ). We have to integrate over the set of all orientations $\Omega \equiv \{0 < \psi < \pi, 0 < \phi < 2\pi\}$ (with $\mathrm{d}\omega \equiv \sin\psi \mathrm{d}\psi\mathrm{d}\phi$), as

$$\sin\psi \mathrm{d}\psi \int_0^{2\pi} \mathrm{d}\phi I_p^{\mathrm{x}}(q) = q^2 \int_\Omega \mathrm{d}\omega I^{\mathrm{x}}(q,\omega). \qquad (11)$$

In detail, considering the expressions for the different cases, we have

$$I_p^{\mathrm{a}}(q) = q^2 \sum_{\boldsymbol{h}\in\Lambda^*} |F(\boldsymbol{h})|^2 \int_\Omega \mathrm{d}\omega \tilde{S}^2(\boldsymbol{q}-\boldsymbol{h}); \qquad (12)$$

$$I_p^{\mathrm{b}}(q) = q^2 \sum_{\boldsymbol{h}\in\Lambda^*} \int_\Omega \mathrm{d}\omega\, |F(\boldsymbol{q})|^2 \tilde{S}^2(\boldsymbol{q}-\boldsymbol{h}); \qquad (13)$$

$$I_p^{\mathrm{c}}(q) = q^2 \sum_{\boldsymbol{h}\in\Lambda^*} |F(\boldsymbol{h},q)|^2 \int_\Omega \mathrm{d}\omega \tilde{S}^2(\boldsymbol{q}-\boldsymbol{h}). \qquad (14)$$

The integration in case b) is much more difficult and it cannot generally be expressed in closed form even for simple shapes. Therefore, as a careful implementation of form c) is at least as good a description as form b), we shall disregard b) in the following. Suppose now that G is a sphere of radius R and volume $V = 4\pi R^3/3$, we have

$$\tilde{S}(\boldsymbol{q}) = \tilde{S}(q) = 3V\left[\frac{\sin(y) - y\cos(y)}{y^3}\right]_{y=2\pi qR} \qquad (15)$$

and, as $|\boldsymbol{q}-\boldsymbol{h}| = (q^2 + h^2 - 2qh\cos\psi)^{1/2}$,

$$\tilde{S}(\boldsymbol{q}-\boldsymbol{h}) = 3V\left[\frac{\sin(y) - y\cos(y)}{y^3}\right] \qquad (16)$$
$$\text{with} \quad y = 2\pi(q^2 + h^2 - 2qh\cos\psi)^{1/2}R.$$

Substituting in Eqs. (12,14) yields[31]

$$I_p^{\mathrm{a}}(q) = \frac{3qVR}{8\pi} \sum_{\boldsymbol{h}\in\Lambda^*} |F(\boldsymbol{h})|^2 \frac{(A_- - A_+)}{h}; \qquad (17)$$

$$I_p^{\mathrm{c}}(q) = \frac{3qVR}{8\pi} \sum_{\boldsymbol{h}\in\Lambda^*} |F(\boldsymbol{h},q)|^2 \frac{(A_- - A_+)}{h}, \qquad (18)$$

$$\text{where} \quad A_\pm \equiv y^{-2}\left(1 - \sin(2y)/y + \sin^2(y)/y^2\right)$$
$$\text{for} \quad y = 2\pi R(q \pm h).$$

Now we consider the crystal's Laue group $\mathcal{G}$ so that we can extend the summation on the asymmetric part $\Lambda^*/\mathcal{G}$ of the reciprocal lattice:

$$I_p^{\mathrm{a}}(q) = \frac{3qVR}{8\pi} \sum_{\boldsymbol{h}\in\Lambda^*/\mathcal{G}} \mu_{\boldsymbol{h}} |F(\boldsymbol{h})|^2 \frac{(A_- - A_+)}{h}; \qquad (19)$$

$$I_p^{\mathrm{c}}(q) = \frac{3qVR}{8\pi} \sum_{\boldsymbol{h}\in\Lambda^*/\mathcal{G}} \mu_{\boldsymbol{h}} |F(\boldsymbol{h},q)|^2 \frac{(A_- - A_+)}{h}, \qquad (20)$$

where $\mu_{\boldsymbol{h}}$ is the multiplicity of $\boldsymbol{h}$ subject to $\mathcal{G}$. Evaluation of $I_p^{\mathrm{c}}(q)$ is only slightly more complex than $I_p^{\mathrm{a}}(q)$, and the gain in accuracy justifies the effort.

We have computed test patterns to compare forms a) and c), considering NPs of diameter $\approx 10a$, being this the lower size limit of validity of the shape-based approach.

We have considered Au spherical NPs of diameter 5 nm (a=0.40786 nm, λ=0.154056 nm, $2\theta = 20^{\rm o}\ldots150^{\rm o}$, Lorentz correction and Debye-Waller factor $\exp(-Bq^2/2)$, with $B = 0.005$ nm^2). The powder pattern was calculated exactly by the Debye sum[10,15] and by Eqs. (19,20). The profiles showed in Fig. 1a are calculated on an absolute scale. They match quite well, but a maximum error $\approx 2-3\%$ is present in both cases a,c. The profile wR agreement index between $I_p^{\rm Debye}$ and $I_p^{\rm c}$ is 3.1%, between $I_p^{\rm Debye}$ and $I_p^{\rm a}$ is wR=4.4%. The difference profiles (Fig. 1b) show that $I_p^{\rm Debye}-I_p^{\rm c}$ has a similar shape to $I_p^{\rm Debye}$, while $I_p^{\rm Debye}-I_p^{\rm a}$ is quite different. Accordingly, refining a scale factor between $I_p^{\rm Debye}$ and $I_p^{\rm c}$ lowers wR to 2.0% (with featureless difference, Fig. 1c), while a scale factor between $I_p^{\rm Debye}$ and $I_p^{\rm a}$ yields wR=3.5%, with still a characteristic difference profile. Furthermore, the peak positions result very little shifted ($< 0.002^{\rm o}$) between $I_p^{\rm Debye}$ and $I_p^{\rm c}$, while they are shifted up to $0.04^{\rm o}$ between $I_p^{\rm Debye}$ and $I_p^{\rm a}$ (Fig. 1d).

Then, we have considered ZnSe spherical NPs of diameter 4.8 nm (a=0.5633 nm, λ=0.154056 nm, $2\theta = 20^{\rm o}\ldots135^{\rm o}$, Lorentz correction and Debye-Waller factor with $B = 0.005$ nm^2). Once more, the powder pattern was calculated exactly by the Debye sum[10,15] and by Eqs. (19,20). The profiles - calculated on an absoulte scale (Fig. 2a) - match quite well with a maximum error $\approx 1-2\%$ for both cases a,c. The profile agreement index wR between $I_p^{\rm Debye}$ and $I_p^{\rm c}$ is 1.8%, between $I_p^{\rm Debye}$ and $I_p^{\rm a}$ is wR=3.1%. The difference profiles (Fig. 2b) show again that $I_p^{\rm Debye}-I_p^{\rm c}$ has a similar shape to $I_p^{\rm Debye}$, while $I_p^{\rm Debye}-I_p^{\rm a}$ is quite different. Accordingly, we have refined again a scale factor (and this time also a different Debye-Waller factor B) between $I_p^{\rm Debye}$ and $I_p^{\rm c}$. wR decreases to 1.6% with featureless difference (Fig. 2c). On the opposite, when refining scale factor and Debye-Waller factor between $I_p^{\rm Debye}$ and $I_p^{\rm a}$ the agreement index does not go below wR=3.1%. Also the difference profile is little changed (Fig. 2c). Again, the peak positions result very little shifted ($< 0.001^{\rm o}$) between $I_p^{\rm Debye}$ and $I_p^{\rm c}$, while peak shifts up to $0.05^{\rm o}$ between $I_p^{\rm Debye}$ and $I_p^{\rm a}$ are visible (Fig. 2d). Form c) again turns out to be less affected than a) by neglecting the cross-term $\mathcal{R}$. A small variation of the Debye-Waller factor (from 0.005 to 0.0047 nm^2) is due to the fact that the $\mathcal{R}$-neglection error changes slightly the intensity ratios. This is however less troublesome than the peak shifts observed for form a).

It results that at NP diameters $D \approx 10a$ the errors in the shape-based diffraction pattern calculations, whatever form we choose, start to be evident. This approach should not be used below this threshold. Also, form a) - which is the standard choice for large particles - shows a much larger error and should be avoided in favor of c).

D. The log-normal size distribution

There are several experimental and theoretical reasons[34] to believe that NP powders have a log-normal distribution of NP size. The log-normal distribution of NP radii is usually written in terms of its mode R_m and width w_R, as

$$L(R) = \frac{1}{w_R\sqrt{2\pi}}\exp\left\{-\frac{[\log(R)-\log(R_m)]^2}{2w_R^2}\right\}. \quad (21)$$

The most direct information on a distribution is provided by the distribution-averaged NP radius R_{ave} and the relevant standard deviation σ_R. For a log-normal, the latter parameters are related to the former by

$$R_{ave} = R_m\exp(w_R^2/2); \qquad \sigma_R = R_m^2\exp(2w_R^2); \quad (22)$$

and

$$\begin{aligned} R_m &= \frac{1}{\sqrt{1+\sigma_R^2/R_{ave}^2}}; \\ w_R &= \sqrt{\log\left(1+\sigma_R^2/R_{ave}^2\right)}. \end{aligned} \quad (23)$$

We shall use a form depending directly on R_{ave}, σ_R[35]. Setting two adimensional parameters $\rho = R/R_{ave}$, $c = 1+\sigma_R^2/R_{ave}^2$, we have

$$L(R) = \frac{1}{R\sqrt{2\pi\log(c)}}\exp\left[-\frac{\log^2(\rho\sqrt{c})}{2\log(c)}\right]. \quad (24)$$

Volume- and area-averaged NP diameters can be derived by

$$D_V = \frac{3}{2}R_{ave}c^3; \qquad D_A = \frac{4}{3}R_{ave}c^2. \quad (25)$$

III. NANOCRYSTALLINE CERIA

A. Experimental

X-ray powder diffraction patterns of a nanocrystalline 20-nm CeO_2 sample, available for a round-robin[35], were downloaded (`http://www.boulder.nist.gov/div853/balzar/`, `http://www.du.edu/~balzar/s-s_rr.htm`). The NP size is well inside the limits of validity of the shape-based method. Among the available datasets, the selected raw data were collected at the NSLS X3B1 beamline of the Brookhaven National Laboratory in flat-plate geometry, with a double-crystal Si(111) monochromator on the incident beam ($\lambda = 0.6998$ Å, $2\theta = 12^{\rm o}(0.01^{\rm o})60^{\rm o}$) and a Ge(111) analyzer crystal on the diffracted beam.

B. Data preprocessing

Three data preprocessing stages have been accomplished. First, the instrumental function has been de-

convoluted by an original advanced technique, including denoising and background subtraction, described in Ref. 36.

Secondly, the pattern has been fitted by generic asymmetric Voigt profiles so as to obtain information about peak positions and intensities. By comparing the intensities as evaluated from the fit with the theoretical ones a small correction for texture and/or microabsorption has been evaluated. The intensity corrections so obtained have then been stored and used in the subsequent stages.

Finally, the peak positions were found to be slightly anisotropically shifted. This has been attributed to a small residual stress, due *e.g.* to dislocations. To confirm this point, we have evaluated the average lattice spacing variations $[\Delta d/d]_{\boldsymbol{h}} = -\frac{\pi}{360}\cot(\theta_{\boldsymbol{h}})\Delta(2\theta_{\boldsymbol{h}})$ for all single reflections $\boldsymbol{h}$. Then we have compared those values with a simple model of elastic anisotropy[37]. They resulted in good agreement. In Fig. 3 we show the fit of $[\Delta d/d]_{\boldsymbol{h}}$'s with Eq. (28) of Ref. 37. The magnitudes of the residual stress tensor components, at least for those which can be determined in this way, resulted to be in the range 1–10 MPa. The values of $|\Delta(2\theta_{\boldsymbol{h}})|$ are below $0.005^{\rm o}$, and $[\Delta d/d]_{\boldsymbol{h}}$ range in $1\text{–}7\times10^{-4}$, which are quite small values. As the strain broadening is of the same order of magnitude of the peak shifts[38], we can confirm that strain broadening is rather small in the CeO_2 sample and can be neglected, as in Ref. 35. Also the residual-stress peak shifts so obtained have been saved as fixed corrections for the subsequent stages.

C. Full-pattern refinement

The total intensity diffracted by the powder NP sample is described by the sum

$$I^{cal}(q) = I^{bkg}(q) + \sum_{k=0}^{k_{max}} L(R_k) I_k(q), \qquad (26)$$

where $R_k = (k + 1/2)\Delta R$, $k = 1 \ldots k_{max}$; $I_k(q)$ is $I_p^c(q)$ of Eq. (20) evaluated at $R = R_k$; and $I^{bkg}(q)$ is a polynomial modelling the background. The step $\Delta R = a(2\pi/3)^{-1/3}$ is chosen so as to have an integer number of atoms in each k-th x-ray sphere of radius R_k, while keeping the point density constant and preserving stoichiometry. It is evidently possible to use a size-dependent lattice parameter a_k in the calculation of $I_k(q)$. For this sample this has been deemed unnecessary. Indeed, for diameters of 20 nm, the lattice parameter of CeO_2 has been found[39] to be already equal to the bulk value. A least-square full-pattern refinement means minimizing the quantity

$$\chi^2 = \sum_{i=1}^{N_{obs}} \left(I^{cal}(q_i) - I_i^{obs}\right)^2 w_i. \qquad (27)$$

Here I_i^{obs} is the i-th point of the experimental pattern corresponding to the scattering vector q_i, N_{obs} the number of experimental points and the weights w_i are the estimated inverse variance of the observations. The refined parameters are: the average NPs radius (R_{ave}) and the radius dispersion σ_R, the isotropic Debye-Waller factors B for O and Ce atoms, the cubic unit cell parameter a and seven background coefficients. For the minimization, we have used (for this work) a modified simplex algorithm[40], which is robust but time-consuming; however, computing times were reasonable. A derivative-based algorithm (Newton, in progress) should give a handsome acceleration.

The final results are given in Tab. I, together with the corresponding values of Ref. 35. The Debye-Waller factors result to $B_{Ce} = 0.0065$ nm^2 and $B_O = 0.0084$ nm^2. The calculated profile is plotted in Fig. 4 with the experimental pattern and the profile difference. The excellent fit quality and the final GoF value (1.21) indicate the achievement of a reliable result. Indeed, the estimated parameters are in good agreement with Ref. 35. The slight discrepancy (≈ 0.2 nm), larger than standard deviations, might be explained by the improved deconvolution method here applied and by the use of the whole pattern instead of a limited number of peaks as in Ref. 35.

TABLE I: Comparison of size distribution results. Standard deviations are in brackets. Units are nm.

	This work		Ref. 35	
R_{ave}	9.58	(0.02)	9.33	(0.07)
σ_R	4.138	(0.003)	3.92	–
σ_R^2/R_{ave}^2	0.1866	(0.0008)	0.177	0.003
D_V	24.01	(0.02)	22.8	(0.4)
D_A	17.98	(0.02)	17.2	(0.2)

IV. CONCLUSIONS

The method of shape-convolution to calculate the diffraction pattern of NP powders has been thoroughly discussed with respect to its limits of validity. Concerns in applying this method below its optimal size range have been demonstrated theoretically and by simulated patterns. Finally, the effectiveness of full-pattern powder data analysis based on the shape-convolution method was proved to obtain precise size distribution information on NP powder samples with a log-normal distribution of spherical crystallites.

* On leave fromConsiglio Nazionale delle Ricerche, Istituto di Cristallografia (CNR-IC), Via Amendola 122/O, I-70126 Bari, Italy.
† Electronic address: cinzia.giannini@ic.cnr.it

[1] O. Masala and R. Seshadri, Annu. Rev. Mater. Res. **34**, 41 (2004).
[2] S. Ino, J. Phys. Soc. Japan **21**, 346 (1966).
[3] S. Ino and S. Ogawa, J. Phys. Soc. Japan **22**, 1365 (1967).
[4] S. Ino, J. Phys. Soc. Japan **26**, 1559 (1969).
[5] S. Ino, J. Phys. Soc. Japan **27**, 941 (1969).
[6] L. D. Marks, Rep. Prog. Phys. **57**, 603 (1994).
[7] W. Vogel, J. Bradley, O. Vollmer, and I. Abraham, J. Phys. Chem. B **102**, 10853 (1998).
[8] D. Zanchet, B. H. Hall, and D. Ugarte, J. Phys. Chem. B **104**, 11013 (2000).
[9] B. D. Hall, J. Appl. Phys. **87**, 1666 (2000).
[10] A. Cervellino, C. Giannini, and A. Guagliardi, J. Appl. Cryst. **36**, 1148 (2003).
[11] A. Cervellino, C. Giannini, A. Guagliardi, and D. Zanchet, Eur. Phys. J. B **41**, 485 (2004).
[12] B. Palosz, E. Grzanka, S. Gierlotka, S. Stel'makh, R. Pielaszek, U. Bismayer, J. Neuefeind, H. Weber, T. Proffen, R. Von Dreele, et al., Z. Kristallogr. **217**, 497 (2002).
[13] B. Palosz, E. Grzanka, S. Stel'makh, S. Gierlotka, R. Pielaszek, U. Bismayer, H. Weber, T. Proffen, and W. Palosz, Interfacial Effects and Novel Properties of Nanomaterials Solid State Phenomena **94**, 203 (2002).
[14] B. Palosz, S. Stel'makh, E. Grzanka, S. Gierlotka, R. Pielaszek, U. Bismayer, S. Werner, and W. Palosz, J. Phys. Cond. Mat. **16**, S353 (2004).
[15] A. Guinier, *X-ray diffraction in crystals, imperfect crystals, and amorphous bodies. Reprint Edition* (Dover Publications:Dover, 1994), chap. 2, pp. 27–54.
[16] A. Cervellino, C. Giannini, and A. Guagliardi (2005), unpublished.
[17] T. Ino and N. Minami, Acta Cryst. A **35**, 163 (1979).
[18] N. Minami and T. Ino, Acta Cryst. A **35**, 171 (1979).
[19] T. Ino and N. Minami, Acta Cryst. A **40**, 538 (1984).
[20] P. Scherrer, Nachr. Ges. Wiss. Göttingen **26**, 98 (1918).
[21] B. E. Warren and B. L. Averbach, J. Appl. Phys. **23**, 497 (1952).
[22] B. E. Warren, *X-ray diffraction* (Addison Wesley:Menlo Park, 1969).
[23] M. Wilkens, Phys. Stat. Sol. A **2**, 359 (1970).
[24] J. I. Langford and A. J. C. Wilson, J. Appl. Cryst. **11**, 102 (1978).
[25] T. Ungár, Á. Révész, and A. Borbély, J. Appl. Cryst. **31**, 554 (1998).
[26] J. I. Langford, D. Louër, and P. Scardi, J. Appl. Cryst. **33**, 964 (2000).
[27] T. Ungár, J. Gubicza, G. Ribárik, and A. Borbély, J. Appl. Cryst. **34**, 298 (2001).
[28] A. Borbély and I. Groma, Appl. Phys. Lett. **79**, 1772 (2001).
[29] D. N. Talwar, M. Vandevyver, K. Kunc, and M. Zigone, Mat. Res. **4**, 71 (2001).
[30] I. C. Dragomir and T. Ungár, J. Appl. Cryst. **35**, 556 (2002).
[31] A. L. Patterson, Phys. Rev. **56**, 972 (1939).
[32] P. P. Ewald, Proc. Phys. Soc. London **52**, 167 (1940).
[33] R. Hosemann and S. N. Bagchi, *Direct analysis of diffraction by matter* (North-Holland:Amsterdam, 1962), pp. 260–264.
[34] L. F. Kiss, J. Söderlund, G. A. Niklasson, and C. G. Granqvist, Nanotechnology **10**, 25 (1999).
[35] D. Balzar, N. Audebrand, M. R. Daymond, A. Fitch, A. Hewat, J. I. Langford, A. Le Bail, D. Louër, O. Masson, C. N. McCowan, et al., J. Appl. Cryst. **37**, 911 (2004).
[36] A. Cervellino, C. Giannini, A. Guagliardi, and M. Ladisa (2005), arXiv:cond-mat/0502582.
[37] N. C. Popa, J. Appl. Cryst. **33**, 103 (2000).
[38] A. K. Singh and C. Balasingh, J. Appl. Phys. **90**, 2296 (2001).
[39] F. Zhang, S. Chan, J. E. Spanier, E. Apak, Q. Jin, R. D. Robinson, and I. P. Herman, Appl. Phys. Lett. **80**, 127 (2002).
[40] J. A. Nelder and R. Mead, Comp. J. **7**, 308 (1965).
[41] C. Giacovazzo, H. L. Monaco, D. Viterbo, F. Scordari, G. Gilli, G. Zanotti, and M. Catti, *Fundamentals of Crystallography* (IUCr-Oxford University Press:Oxford, 1992), chap. 5, pp. 321–324.
[42] Other NP samples (ZnTe, ZnSe) in the 5–20 nm size range have been treated successfully and the results shall be published separately.
[43] We remark here that constructions b) and c) are less dramatically different than what appears in 17, depending on a proper choice of the unit cell. A physically descriptive choice, as the Wigner-Seitz unit cell, for instance, would reduce those differences.
[44] For the sake of brevity we omit the factors v_c^{-1} from the Fourier amplitudes and v_c^{-2} from the related intensities, where v_c is the unit cell volume.

Figures

FIG. 1: (Color online) A model spherical cluster Au_{3925} of 5.0 nm diameter with fcc structure (a=0.40786 nm) has been constructed according to principle c) of Sec. II A. In this case, as the monoatomic fcc Wigner-Seitz unit cell contains one atom, principle c) coincides with b).
a: the powder diffraction pattern: red, exact intensity $I_p^{\rm Debye}(q)$ calculated by the Debye function[15]; blue dotted, $I_p^{\rm a}(q)$ calculated by approach a), Eq. (19); green dashed, $I_p^{\rm c}(q)$calculation by approach c), Eq. (20). All intensities have been calculated on an absolute scale and then scaled by the same factor.
b: lower line, red, difference $I_p^{\rm Debye}(q) - I_p^{\rm c}(q)$; middle line, green, difference $I_p^{\rm Debye}(q) - I_p^{\rm a}(q)$; upper line, blue, the exact powder pattern $\times 1/100$ (Debye method) for comparison.
c: lower line, red, difference $I_p^{\rm Debye}(q) - s\, I_p^{\rm c}(q)$ after refining a scale factor $s = 1.024$; middle line, green, difference $I_p^{\rm Debye}(q) - sI_p^{\rm a}(q)$after refining a scale factor $s = 1.027$; upper line, blue, the exact powder pattern $\times 1/100$ (Debye method) for comparison. Note that the c)-type pattern difference is flattened while the a)-type retains sharp contributions.
d: detail around the (111) peak of the $I_p^{\rm Debye}$ and $I_p^{\rm a}$ patterns (same coding as in part a) after scaling, showing a significant peak shift for the $I_p^{\rm a}$ pattern.

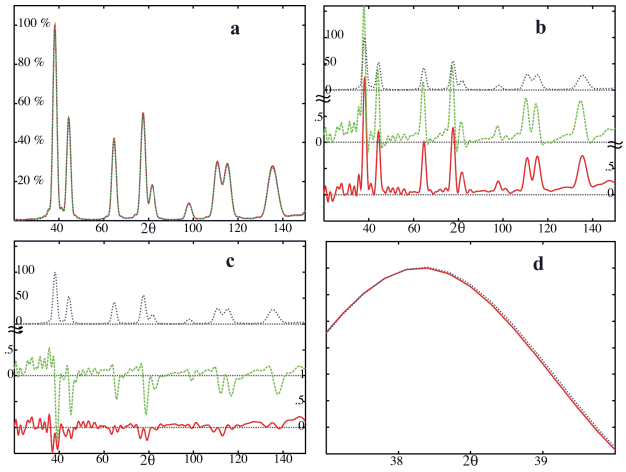


FIG. 2: (Color online) A model spherical cluster $(ZnSe)_{1289}$ of 4.8 nm diameter with fcc structure (a=0.5633 nm) has been constructed according to principle c) of Sec. II A. In this case, as the fcc Wigner-Seitz unit cell contains two atoms, construction c) differs from b).
a: the powder diffraction pattern: red, exact intensity $I_p^{\rm Debye}(q)$ calculated by the Debye function[15]; blue dotted, $I_p^{\rm a}(q)$ calculated by approach a), Eq. (19); green dashed, $I_p^{\rm c}(q)$calculation by approach c), Eq. (20). Again all intensities have been calculated on an absoulte scale.
b: lower line, red, difference $I_p^{\rm Debye}(q) - I_p^{\rm c}(q)$; middle line, green, difference $I_p^{\rm Debye}(q) - I_p^{\rm a}(q)$; upper line, blue, the exact powder pattern $\times 1/100$ (Debye method) for comparison.
c: lower line, red, difference $I_p^{\rm Debye}(q) - s\, I_p^{\rm c}(q)$ after refining a scale factor $s = 0.999$ and an overall-isotropic Debye-Waller factor $B = 0.468$ ($I_p^{\rm Debye}$ has been evaluated with $B = 0.5$); middle line, green, difference $I_p^{\rm Debye}(q) - sI_p^{\rm a}(q)$ after refining a scale factor $s = 0.996$ and $B = 0.467$; upper line, blue, the exact powder pattern $\times 1/100$ (Debye method) for comparison. Note again that the c)-type pattern difference is flattened while the a)-type retains sharp contributions.
d: detail around the (531) peak of the $I_p^{\rm Debye}$ and $I_p^{\rm a}$ patterns (same coding as in part a) after scaling, showing a significant peak shift for the $I_p^{\rm a}$ pattern.

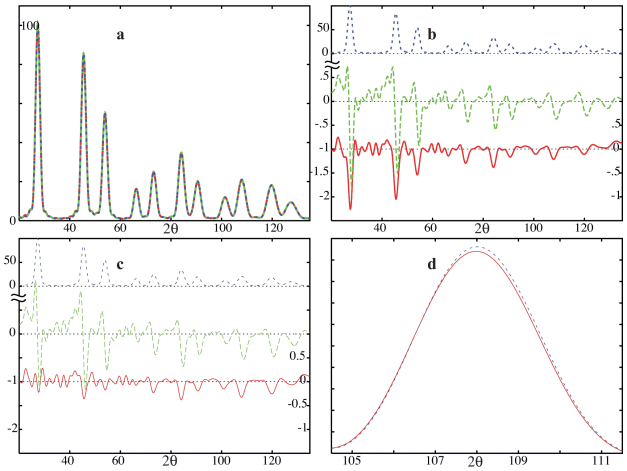


FIG. 3: (Color online) The measured (red error bars) and calculated (blue diamonds) lattice spacing variations for all well-isolated Bragg peaks of CeO_2 plotted against the relevant peaks diffraction angle. Error bars have been evaluated assuming a constant error of 0.0006° on the anisotropic angular peak shift. Calculated values refer to the model of Ref. 37 where residual stress components have been refined.

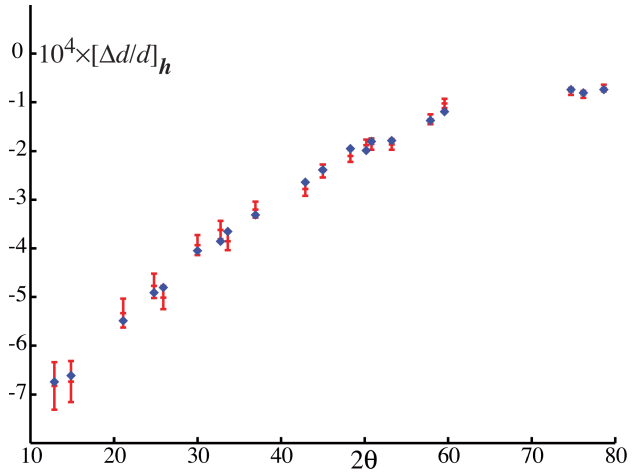
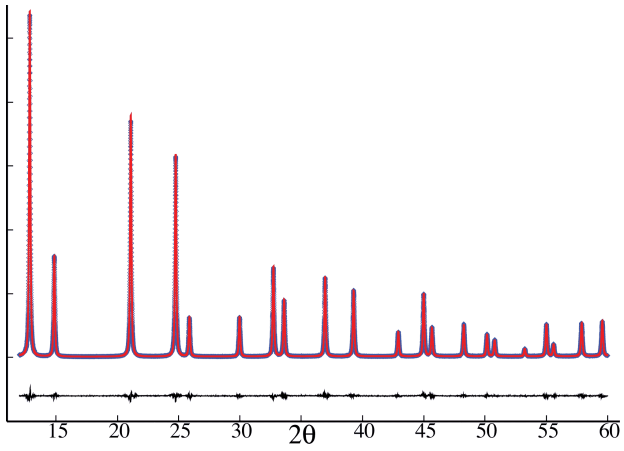


FIG. 4: (Color online) Nanosized CeO_2 powder pattern final fit. Blue diamonds - the observed deconvoluted intensity; red continuous line - the calculated intensity; black continuous line, below - difference profile (same scale).



APPENDIX: ERROR EVALUATION

Assume to deal with particles of centrosymmetric shape $S(\boldsymbol{r}) = S(-\boldsymbol{r})$ and equivalent spherical radius R (*i.e.*, the radius of the sphere of equal volume.). The shape Fourier transform $\tilde{S}(\boldsymbol{q})$ is then a real even function:

$$\tilde{S}(\boldsymbol{q}) = \tilde{S}(-\boldsymbol{q}). \tag{A.1}$$

Recall also that the gradient of an even function is odd:

$$\tilde{\boldsymbol{G}}(\boldsymbol{q}) \equiv \nabla_{\boldsymbol{q}}\tilde{S}(\boldsymbol{q}) = -\tilde{\boldsymbol{G}}(-\boldsymbol{q}). \tag{A.2}$$

Our aim is to evaluate - for the different forms a), b), c) as introduced in Sec. II A and carried out in Sec. II B, Sec. II C - the neglected residual intensity contribution $\mathcal{R}(\boldsymbol{q})$ of Eq. (10) with respect to the respective retained term (*cf.* Eqs. (7,8,9)) in the immediate vicinity of a Bragg peak.

Let $\boldsymbol{h}_0$ the nearest Bragg peak to $\boldsymbol{q}$. First note that, if $|\boldsymbol{q}-\boldsymbol{h}_0| \gg 1/R$, $\mathcal{R}(\boldsymbol{q})$ is of order $(2\pi qR)^{-4}$, so we neglect it altogether. If $\boldsymbol{q}$ is very close to $\boldsymbol{h}_0$, set $\boldsymbol{q} = \boldsymbol{h}_0 + \Delta\boldsymbol{q}$ (so $\Delta q \lesssim 1/R$). We can drop in the sum over $\boldsymbol{h}$ all terms with $\boldsymbol{h} \neq \boldsymbol{h}_0$ because they are $O(2\pi qR)^{-4}$ and reorder the second sum, obtaining

$$\begin{aligned}\mathcal{R}^{\mathrm{a}}(\boldsymbol{h}_0+\Delta\boldsymbol{q}) &\approx \tilde{S}(\Delta\boldsymbol{q}) \sum_{\substack{\boldsymbol{k}\in\Lambda^*\\ \boldsymbol{k}\neq 0}} \tilde{S}(\Delta\boldsymbol{q}+\boldsymbol{k})F(\boldsymbol{h}_0)\times \\ &\times \overline{F}(\boldsymbol{h}_0-\boldsymbol{k})\end{aligned} \tag{A.3}$$

$$\begin{aligned}\mathcal{R}^{\mathrm{b}}(\boldsymbol{h}_0+\Delta\boldsymbol{q}) &\approx \tilde{S}(\Delta\boldsymbol{q})\,|F(\boldsymbol{h}_0+\Delta\boldsymbol{q})|^2 \times \\ &\times \sum_{\substack{\boldsymbol{k}\in\Lambda^*\\ \boldsymbol{k}\neq 0}} \tilde{S}(\Delta\boldsymbol{q}+\boldsymbol{k})\end{aligned} \tag{A.4}$$

$$\begin{aligned}\mathcal{R}^{\mathrm{c}}(\boldsymbol{h}_0+\Delta\boldsymbol{q}) &\approx \tilde{S}(\Delta\boldsymbol{q}) \sum_{\substack{\boldsymbol{k}\in\Lambda^*\\ \boldsymbol{k}\neq 0}} \tilde{S}(\Delta\boldsymbol{q}+\boldsymbol{k})\times \\ &\times F(\boldsymbol{h}_0,q)\overline{F}(\boldsymbol{h}_0-\boldsymbol{k},q) \\ \text{where}\quad & q \equiv |\boldsymbol{h}_0+\Delta\boldsymbol{q}|\end{aligned} \tag{A.5}$$

At the same time, for $\boldsymbol{q} = \boldsymbol{h}_0 + \Delta\boldsymbol{q}$ with $\Delta q \lesssim 1/R$, the intensities $I^{\mathrm{x}}(\boldsymbol{q})$ of Eqs. (7,8,9) can be approximated by the $\boldsymbol{h}_0$-th term of the RHS sum, neglecting terms of $O(2\pi qR)^{-4}$. Furthermore, in general, $\tilde{S}(\Delta\boldsymbol{q}) = \tilde{S}(0) + O(\Delta q^2)$. Therefore, the ratios $\mathcal{R}^{\mathrm{x}}(\boldsymbol{h}_0+\Delta\boldsymbol{q})/I^{x}(\boldsymbol{h}_0+\Delta\boldsymbol{q})$ are given by

$$\begin{aligned}\hat{\mathcal{R}}^{\mathrm{a}}(\boldsymbol{h}_0,\Delta\boldsymbol{q}) &\equiv \frac{\mathcal{R}^{\mathrm{a}}(\boldsymbol{h}_0+\Delta\boldsymbol{q})}{\tilde{S}^2(\Delta\boldsymbol{q})|F(\boldsymbol{h}_0)|^2} \\ &\approx \sum_{\substack{\boldsymbol{k}\in\Lambda^*\\ \boldsymbol{k}\neq 0}} \tilde{s}(\Delta\boldsymbol{q},\boldsymbol{k})\frac{\overline{F}(\boldsymbol{h}_0-\boldsymbol{k})}{\overline{F}(\boldsymbol{h}_0)}\end{aligned} \tag{A.6}$$

$$\begin{aligned}\hat{\mathcal{R}}^{\mathrm{b}}(\boldsymbol{h}_0,\Delta\boldsymbol{q}) &\equiv \frac{\mathcal{R}^{\mathrm{b}}(\boldsymbol{h}_0+\Delta\boldsymbol{q})}{\tilde{S}^2(\Delta\boldsymbol{q})|F(\boldsymbol{h}_0+\Delta\boldsymbol{q})|^2} \\ &\approx \sum_{\substack{\boldsymbol{k}\in\Lambda^*\\ \boldsymbol{k}\neq 0}} \tilde{s}(\Delta\boldsymbol{q},\boldsymbol{k})\end{aligned} \tag{A.7}$$

$$\begin{aligned}\hat{\mathcal{R}}^{\mathrm{c}}(\boldsymbol{h}_0,\Delta\boldsymbol{q}) &\equiv \frac{\mathcal{R}^{\mathrm{c}}(\boldsymbol{h}_0+\Delta\boldsymbol{q})}{\tilde{S}^2(\Delta\boldsymbol{q})|F(\boldsymbol{h}_0,q)|^2} \\ &\approx \sum_{\substack{\boldsymbol{k}\in\Lambda^*\\ \boldsymbol{k}\neq 0}} \tilde{s}(\Delta\boldsymbol{q},\boldsymbol{k})\frac{\overline{F}(\boldsymbol{h}_0-\boldsymbol{k},q)}{\overline{F}(\boldsymbol{h}_0,q)} \\ \text{where}\qquad & \tilde{s}(\Delta\boldsymbol{q},\boldsymbol{k}) \equiv \frac{\tilde{S}(\Delta\boldsymbol{q}+\boldsymbol{k})}{\tilde{S}(0)}\end{aligned} \tag{A.8}$$

Note that, because of Eqs. (A.1,A.2), we have

$$\tilde{s}(\Delta\boldsymbol{q},\boldsymbol{k}) = \tilde{s}(-\Delta\boldsymbol{q},-\boldsymbol{k}); \tag{A.9}$$

$$\begin{aligned}\tilde{\boldsymbol{g}}(\Delta\boldsymbol{q},\boldsymbol{k}) &\equiv \nabla_{\Delta\boldsymbol{q}}\tilde{s}(\Delta\boldsymbol{q},\boldsymbol{k}) = \tilde{\boldsymbol{G}}(\Delta\boldsymbol{q}+\boldsymbol{k})/\tilde{S}(0) \\ &= -\tilde{\boldsymbol{g}}(-\Delta\boldsymbol{q},-\boldsymbol{k}).\end{aligned} \tag{A.10}$$

We can immediately veryfy that in case b) it results

$$\nabla_{\Delta\boldsymbol{q}}\hat{\mathcal{R}}^{\mathrm{b}}(\boldsymbol{h}_0,\Delta\boldsymbol{q}) = \sum_{\substack{\boldsymbol{k}\in\Lambda^*\\ \boldsymbol{k}\neq 0}} \tilde{\boldsymbol{g}}(\Delta\boldsymbol{q},\boldsymbol{k}) \tag{A.11}$$

In the sum above the term with index $\boldsymbol{k}$ is always accompanied by a term with index $-\boldsymbol{k}$. Setting also $\Delta\boldsymbol{q} = 0$, and using Eq. (A.10), we have

$$\nabla_{\Delta\boldsymbol{q}}\hat{\mathcal{R}}^{\mathrm{b}}(\boldsymbol{h}_0,0) = \sum_{\boldsymbol{k}\in\Lambda^*/2} (\tilde{\boldsymbol{g}}(0,\boldsymbol{k}) + \tilde{\boldsymbol{g}}(0,-\boldsymbol{k})) = 0\,. \tag{A.12}$$

where $\Lambda^*/2$ denotes an arbitrarily chosen half-space of the reciprocal lattice without the origin. Now, expanding $\hat{\mathcal{R}}^{\mathrm{b}}(\boldsymbol{h}_0,\Delta\boldsymbol{q})$ in Taylor series at $\Delta\boldsymbol{q} = 0$, we have

$$\hat{\mathcal{R}}^{\mathrm{b}}(\boldsymbol{h}_0,\Delta\boldsymbol{q}) \approx \hat{\mathcal{R}}^{\mathrm{b}}(\boldsymbol{h}_0,0) + O(\Delta q^2). \tag{A.13}$$

Note also in Eq. (A.7) that $\hat{\mathcal{R}}^{\mathrm{b}}(\boldsymbol{h}_0,0)$ does not depend on the considered Bragg reflection $\boldsymbol{h}_0$. Therefore, we can write

$$\mathcal{R}^{\mathrm{b}}(\boldsymbol{q}) \propto I^{\mathrm{b}}(\boldsymbol{q}), \tag{A.14}$$

and the proportionality constant can be evaluated by Eq. (A.7) with $\Delta\boldsymbol{q} = 0$. We can conclude that the effect of neglecting $\mathcal{R}^{\mathrm{b}}$ will be just a relative error on the global profile scale factor. This factor is size-dependent, however, therefore for size distribution analysis at small sizes it may be necessary to introduce a correction as from Eq. (A.7).

Cases a), c), are more complex. We are interested to powder diffraction, where $I(\boldsymbol{q})$ is to be integrated at constant q, therefore we shall consider

$$\overline{\mathcal{R}}^{\mathrm{x}}(\boldsymbol{h}_0,\Delta\boldsymbol{q}) = \frac{1}{2}\left[\hat{\mathcal{R}}^{\mathrm{x}}(\boldsymbol{h}_0,\Delta\boldsymbol{q}) + \hat{\mathcal{R}}^{\mathrm{x}}(-\boldsymbol{h}_0,-\Delta\boldsymbol{q})\right] \tag{A.15}$$

Expanding $\overline{\mathcal{R}}^{\rm x}(\boldsymbol{h}_0,\Delta\boldsymbol{q})$ in Taylor series at $\Delta\boldsymbol{q}=0$, we have

$$\overline{\mathcal{R}}^{\rm x}(\boldsymbol{h}_0,\Delta\boldsymbol{q}) \approx \overline{\mathcal{R}}^{\rm x}(\boldsymbol{h}_0,0) + \nabla_{\Delta\boldsymbol{q}}\overline{\mathcal{R}}^{\rm x}(\boldsymbol{h}_0,0)\cdot\Delta\boldsymbol{q} + O(\Delta q^2). \tag{A.16}$$

We shall now develop $\overline{\mathcal{R}}^{\rm a}(\boldsymbol{h}_0,\Delta\boldsymbol{q})$ and $\nabla_{\Delta\boldsymbol{q}}\overline{\mathcal{R}}^{\rm a}(\boldsymbol{h}_0,0)$ in cases a, c.

1. Case c)

First, recall that the atomic form factors $f_\alpha(q)$ are constants for neutron scatering and monotonically decreasing smooth functions in the x-ray case. In the latter case, furthermore, the form factors of different elements have remarkably similar profiles. For a structure with N_a atoms in the unit cell, it is then possible[41] to approximate

$$f_\alpha(q) \approx c_\alpha \langle f(q)\rangle \equiv c_\alpha \frac{1}{N_a}\sum_{\beta=1}^{N_a} f_\beta(q). \tag{A.17}$$

with c_α appropriate constants. Therefore the structure factor ratios appearing in Eq. (A.8) can be simplified as

$$\frac{\overline{F}(\boldsymbol{h}_0-\boldsymbol{k},q)}{\overline{F}(\boldsymbol{h}_0,q)} \approx \frac{\sum_{\alpha=1}^{N_a} c_\alpha {\rm e}^{-2\pi i(\boldsymbol{h}_0-\boldsymbol{k})\cdot\boldsymbol{r}_\alpha}}{\sum_{\beta=1}^{N_a} c_\beta {\rm e}^{-2\pi i\boldsymbol{h}_0\cdot\boldsymbol{r}_\beta}} \equiv \tau(\boldsymbol{h}_0,\boldsymbol{k}), \tag{A.18}$$

independent of $q=|\boldsymbol{h}_0+\Delta\boldsymbol{q}|$. Note that

$$\tau(-\boldsymbol{h}_0,-\boldsymbol{k}) = \overline{\tau}(\boldsymbol{h}_0,\boldsymbol{k}); \qquad \tau(-\boldsymbol{h}_0,\boldsymbol{k}) = \overline{\tau}(\boldsymbol{h}_0,-\boldsymbol{k}). \tag{A.19}$$

Now we can write explicitly $\overline{\mathcal{R}}^{\rm c}$ using Eqs. (A.8,A.15) and

$$\begin{aligned}\overline{\mathcal{R}}^{\rm c}(\boldsymbol{h}_0,\Delta\boldsymbol{q}) \;=\; & \frac{1}{2}\sum_{\substack{\boldsymbol{k}\in\Lambda^*\\ \boldsymbol{k}\neq 0}} [\tilde{s}(\Delta\boldsymbol{q},\boldsymbol{k})\tau(\boldsymbol{h}_0,\boldsymbol{k}) + \\ & + \tilde{s}(-\Delta\boldsymbol{q},\boldsymbol{k})\overline{\tau}(\boldsymbol{h}_0,-\boldsymbol{k})]\,. \end{aligned} \tag{A.20}$$

Splitting the sum, reordering $\boldsymbol{k}\to-\boldsymbol{k}$ in one part, using Eq. (A.9) and recombining, we have

$$\overline{\mathcal{R}}^{\rm c}(\boldsymbol{h}_0,\Delta\boldsymbol{q}) = \sum_{\substack{\boldsymbol{k}\in\Lambda^*\\ \boldsymbol{k}\neq 0}} \tilde{s}(\Delta\boldsymbol{q},\boldsymbol{k}){\rm Re}\,[\tau(\boldsymbol{h}_0,\boldsymbol{k})]\,. \tag{A.21}$$

Again as in Eq. (A.12), we can pair terms with $\boldsymbol{k}$ and $-\boldsymbol{k}$. Using Eq. (A.19), we obtain

$$\begin{aligned}\overline{\mathcal{R}}^{\rm c}(\boldsymbol{h}_0,\Delta\boldsymbol{q}) \;=\; & \sum_{\boldsymbol{k}\in\Lambda^*/2} {\rm Re}\,[\tilde{s}(\Delta\boldsymbol{q},\boldsymbol{k})\tau(\boldsymbol{h}_0,\boldsymbol{k}) + \\ & + \tilde{s}(\Delta\boldsymbol{q},-\boldsymbol{k})\tau(\boldsymbol{h}_0,-\boldsymbol{k})]\,. \end{aligned} \tag{A.22}$$

Define now the arbitrary half-lattice $\Lambda^*/2$ as that defined by a plane $\perp\boldsymbol{h}_0$ passing through the origin and containing $\boldsymbol{h}_0$. The origin is excluded. We have

$$\overline{\mathcal{R}}^{\rm c}(\boldsymbol{h}_0,0) = \sum_{\boldsymbol{k}\in\Lambda^*/2} \tilde{s}(0,\boldsymbol{k}){\rm Re}\,[\tau(\boldsymbol{h}_0,\boldsymbol{k})+\tau(\boldsymbol{h}_0,-\boldsymbol{k})]\,. \tag{A.23}$$

Then, evaluating the gradient in $\Delta\boldsymbol{q}=0$, using Eq. (A.2), we have finally

$$\begin{aligned}\nabla_{\Delta\boldsymbol{q}}\overline{\mathcal{R}}^{\rm c}(\boldsymbol{h}_0,0) \;=\; & \sum_{\boldsymbol{k}\in\Lambda^*/2} \tilde{\boldsymbol{g}}(0,\boldsymbol{k}) \times \\ & \times\; {\rm Re}\,[\tau(\boldsymbol{h}_0,\boldsymbol{k})-\tau(\boldsymbol{h}_0,-\boldsymbol{k})]\,. \end{aligned} \tag{A.24}$$

The gradient $\nabla_{\Delta\boldsymbol{q}}\overline{\mathcal{R}}^{\rm c}(\boldsymbol{h}_0,0)$ is a vector. We have to take its angular average to determine the effect on the powder pattern. This is done by simply taking the scalar product with $\widehat{\boldsymbol{h}}_0\equiv\boldsymbol{h}_0/h_0$:

$$\begin{aligned}\nabla_{\Delta\boldsymbol{q}}\overline{\mathcal{R}}^{\rm c}(\boldsymbol{h}_0,0)\cdot\widehat{\boldsymbol{h}}_0 \;=\; & \sum_{\boldsymbol{k}\in\Lambda^*/2} (\tilde{\boldsymbol{g}}(0,\boldsymbol{k})\cdot\widehat{\boldsymbol{h}}_0) \times \\ & \times\; {\rm Re}\,[\tau(\boldsymbol{h}_0,\boldsymbol{k})-\tau(\boldsymbol{h}_0,-\boldsymbol{k})]\,. \end{aligned} \tag{A.25}$$

For spherical shape, it will be $\tilde{\boldsymbol{g}}(0,\boldsymbol{k})||\boldsymbol{k}$; therefore terms with $\boldsymbol{k}\perp\boldsymbol{h}_0$ will be zero and those with $\boldsymbol{k}||\boldsymbol{h}_0$ will be most important. Both $\tilde{\boldsymbol{g}}(0,\boldsymbol{k})$ and $\tilde{s}(0,\boldsymbol{k})$ are damped oscillatory functions with amplitude $\sim(2\pi kR)^{-2}$. As $1/a\lesssim k$, the magnitudes of both $\overline{\mathcal{R}}^{\rm c}(\boldsymbol{h}_0,0)$ and $\nabla_{\Delta\boldsymbol{q}}\overline{\mathcal{R}}^{\rm c}(\boldsymbol{h}_0,0)$ are of order $(a/R)^2$. Unfortunately, Eq. (A.25) cannot be estimated more in detail, because of the dependence from the 'reduced' structure factors $\tau(\boldsymbol{h}_0,\boldsymbol{k})$. However, we can assess that its importance would be smaller than the corresponding term for case a) for x-ray scattering.

2. Case a)

In case a), we can trace the same steps as in case c) but instead of the 'reduced' structure factors $\tau(\boldsymbol{h}_0,\boldsymbol{k})$ we have to consider the ratios

$$\zeta(\boldsymbol{h}_0,\boldsymbol{k}) = \frac{\overline{F}(\boldsymbol{h}_0-\boldsymbol{k})}{\overline{F}(\boldsymbol{h}_0)} = \frac{\overline{F}(\boldsymbol{h}_0-\boldsymbol{k})F(\boldsymbol{h}_0)}{|F(\boldsymbol{h}_0)|^2} \tag{A.26}$$

and in the analog sums of Eq. (A.23) and Eq. (A.25) for $\overline{\mathcal{R}}^{\rm a}(\boldsymbol{h}_0,0)$ and $\nabla_{\Delta\boldsymbol{q}}\overline{\mathcal{R}}^{\rm a}(\boldsymbol{h}_0,0)$ there will appear terms as

$${\rm Re}\,[\zeta(\boldsymbol{h}_0,\boldsymbol{k})\pm\zeta(\boldsymbol{h}_0,-\boldsymbol{k})]\,. \tag{A.27}$$

The most important terms for the powder pattern are again those with $\boldsymbol{k}||\boldsymbol{h}_0$. The structure factors $F(\boldsymbol{h}_0\pm\boldsymbol{k})$ (see Eq. (5)) depend on form factors $f_\alpha(|\boldsymbol{h}_0\pm\boldsymbol{k}|)$, and for $\boldsymbol{k}||\boldsymbol{h}_0$ these will be strongly different. This in turn will amplify the differences $\xi(\boldsymbol{h}_0,\boldsymbol{k})$. Therefore it is likely that for case a) the effect of the neglected term $\mathcal{R}^{\rm a}$ will be significantly larger than for case c). The examples reported in Sec. II C show just that.